



Available online at [www.sciencedirect.com](http://www.sciencedirect.com)

**ScienceDirect**

Comput. Methods Appl. Mech. Engrg. 337 (2018) 458–480

**Computer methods  
in applied  
mechanics and  
engineering**

[www.elsevier.com/locate/cma](http://www.elsevier.com/locate/cma)

# The MITC3+ shell element enriched in membrane displacements by interpolation covers

Hyungmin Jun<sup>a</sup>, Kyungho Yoon<sup>b</sup>, Phill-Seung Lee<sup>c,\*</sup>, Klaus-Jürgen Bathe<sup>d</sup>

<sup>a</sup>Department of Biological Engineering, Massachusetts Institute of Technology, Cambridge, MA 02139, USA

<sup>b</sup>Department of Radiology, Brigham and Women's Hospital, Harvard Medical School, Boston, MA 02115, USA

<sup>c</sup>Department of Mechanical Engineering, Korea Advanced Institute of Science and Technology, Daejeon 34141, Republic of Korea

<sup>d</sup>Department of Mechanical Engineering, Massachusetts Institute of Technology, Cambridge, MA 02139, USA

Received 23 December 2017; received in revised form 2 April 2018; accepted 3 April 2018

Available online 9 April 2018

## Abstract

In this paper, we significantly improve the membrane behavior of the previously published 3-node triangular MITC3+ shell element through the use of interpolation covers. We give the formulation of the improved MITC3+ element for linear and nonlinear large displacement analyses. The 3-node shell element passes the basic tests, namely the isotropy, patch, and zero energy mode tests, and we illustrate the excellent performance of the element in various standard test problems.

© 2018 Elsevier B.V. All rights reserved.

**Keywords:** 3-node shell element; Membrane behavior; Assumed strain method; MITC technique; Interpolation covers; Linear and large displacement analyses

## 1. Introduction

For several decades, the development of efficient shell finite elements has been an important research field to advance the finite element method. Major progress has been achieved for 4-node quadrilateral shell finite elements. However, the development of effective 3-node triangular shell elements has been more difficult [1–5].

For bending-dominated shell problems, the finite element solutions frequently deteriorate because the finite element discretization cannot accurately approximate the pure bending displacement fields. This phenomenon is called locking [6–10]. In general, 3-node shell elements are free from membrane locking at the element level due to their flat geometry. However, transverse and in-plane shear locking occur in out-of-plane and in-plane bending cases, respectively. That is, undesirable overly stiff bending and membrane behaviors are observed in the finite element solutions.

Various methods have been proposed to alleviate locking (see Refs. [1–9,11–18] and the references therein). Broadly speaking, the techniques can be referred to as reduced integration, assumed strain, enhanced strain and

\* Corresponding author.

E-mail address: [phillseung@kaist.edu](mailto:phillseung@kaist.edu) (P.S. Lee).

strain smoothing methods. Among these schemes the MITC (Mixed Interpolation of Tensorial Component) procedure, closely related to assumed strain methods, has been successfully used to formulate effective plate and shell elements. In particular, an almost optimal 4-node shell element was proposed [18]. Also, the 3-node MITC3+ triangular shell element was developed and its performance was evaluated in linear and nonlinear analyses [2–4]. However, while this element is quite effective for the analysis of bending-dominated problems, the in-plane membrane behavior of the element is only that of the displacement-based 3-node shell finite element.

To achieve an improved membrane behavior for a 3-node element is particularly difficult because the two techniques given by the use of incompatible modes and the use of drilling degrees of freedom do not sufficiently improve the element behavior [19–21]. However, the generalization of the finite element method using partition of unity based displacement enrichment schemes provides an additional avenue [22–28]. In this way, an improved 3-node shell element behavior was achieved using the MITC3 element with interpolation covers [29].

The objective in this paper is to improve the membrane behavior of the 3-node MITC3+ shell element by using interpolation covers. The approach is as in Ref. [29] but only the membrane displacements are enriched. Since the MITC3+ element shows excellent performance in the analysis of bending-dominated problems, enriching its membrane behavior should make the element more generally applicable. We derive the formulation of the improved shell element for linear and nonlinear analyses and evaluate its performance in comparison with previously developed shell elements. Our study reveals that the performance of the improved MITC3+ element is excellent in both linear and nonlinear analyses, even when highly distorted meshes are used.

## 2. The formulation of the shell element for linear analysis

In this section, we present the formulation of the improved MITC3+ shell element for linear analysis. The formulation is closely related to the developments in Ref. [29].

### 2.1. Enrichment of the membrane displacement field

For the MITC3+ shell element, the geometry interpolation including the bubble node, see Fig. 1, is given by [2]

$$\bar{\mathbf{x}}(r, s, t) = \sum_{i=1}^3 h_i(r, s) \bar{\mathbf{x}}_i + \frac{t}{2} \sum_{i=1}^4 a_i f_i(r, s) \mathbf{V}_n^i \quad (1a)$$

$$\text{with } h_1 = 1 - r - s, \quad h_2 = r, \quad h_3 = s, \quad a_4 \mathbf{V}_n^4 = \frac{1}{3}(a_1 \mathbf{V}_n^1 + a_2 \mathbf{V}_n^2 + a_3 \mathbf{V}_n^3), \quad (1b)$$

in which  $h_i(r, s)$  is the standard 2D interpolation function of the isoparametric procedure corresponding to node  $i$ ,  $\bar{\mathbf{x}}_i$  is the position vector of node  $i$  defined in the global Cartesian coordinate system,  $a_i$  and  $\mathbf{V}_n^i$  denote the shell thickness and the director vector at node  $i$ , respectively, and  $f_i(r, s)$  are the two-dimensional interpolation functions that include the cubic bubble function  $f_4$ , which is related to the internal node 4.

$$f_1 = h_1 - \frac{1}{3}f_4, \quad f_2 = h_2 - \frac{1}{3}f_4, \quad f_3 = h_3 - \frac{1}{3}f_4, \quad f_4 = 27rs(1 - r - s). \quad (2)$$

Note that, unlike the earlier proposed 3-node MITC3 triangular shell element [1], the MITC3+ shell element has an internal node and the corresponding cubic bubble function in the geometry interpolation.

From (1), the displacement interpolation is obtained directly

$$\bar{\mathbf{u}}(r, s, t) = \sum_{i=1}^3 h_i(r, s) \bar{\mathbf{u}}_i + \frac{t}{2} \sum_{i=1}^4 a_i f_i(r, s) (-\mathbf{V}_2^i \alpha_i + \mathbf{V}_1^i \beta_i), \quad (3)$$

in which  $\bar{\mathbf{u}}_i = [\bar{u}_i \quad \bar{v}_i \quad \bar{w}_i]^T$  is the nodal displacement vector,  $\mathbf{V}_1^i$  and  $\mathbf{V}_2^i$  are the unit vectors orthogonal to  $\mathbf{V}_n^i$  and to each other, and  $\alpha_i$  and  $\beta_i$  are the rotations of the director vector  $\mathbf{V}_n^i$  about  $\mathbf{V}_1^i$  and  $\mathbf{V}_2^i$ , respectively, at node  $i$ .

To enrich the membrane displacements of the element, we proceed as in Ref. [29], see also Refs. [27,28]. The cover  $C_i$  corresponding to node  $i$ , is defined as the elements that connect to node  $i$ , as illustrated in Fig. 2. A partition of unity subordinate to each cover is a set of functions that for every point in the domain under consideration sums to 1. Since the finite element shape functions  $h_i$  form a partition of unity, we can directly introduce piecewise polynomials for the nodal displacements with focus on the membrane displacements.

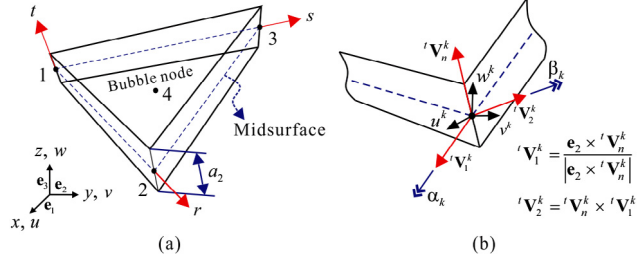


**Fig. 1.** The 3-node shell element with a bubble node: (a) Geometry, (b) Definition of rotational degrees of freedom  $\alpha_k$  and  $\beta_k$ .

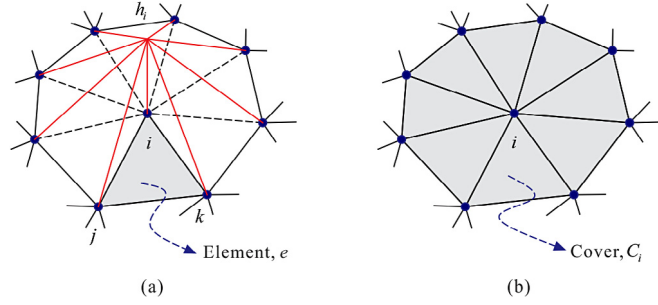


**Fig. 2.** Description of sub-domain: (a) Usual interpolation function  $h_i$  and an element  $e$ , (b) Cover region  $C_i$  constructed by all the elements connected to node  $i$ .

Therefore, the displacement interpolation with the interpolation covers is

$$\mathbf{u}(r, s, t) = \sum_{i=1}^3 h_i(r, s) \mathbf{u}_i^l(\mathbf{x}) + \frac{t}{2} \sum_{i=1}^4 a_i f_i(r, s) (-\mathbf{V}_2^i \alpha_i + \mathbf{V}_1^i \beta_i) \quad \text{with } \mathbf{x} = \sum_{i=1}^3 h_i(r, s) \bar{\mathbf{x}}_i. \quad (4)$$

In the above expression,  $\mathbf{u}_i^l(\mathbf{x})$  is not a nodal displacement vector as in the standard finite element method, but is a vector of displacement functions (with parameters corresponding to node  $i$ ) that are defined over the cover  $C_i$ .

For the local approximation on the cover  $C_i$  given in Eq. (4), we use for the membrane displacements of the shell element

$$\mathbf{u}_i^l(\mathbf{x}) = [a_{0i}^u + (\mathbf{x} \cdot \mathbf{V}_1^i) a_{1i}^u + (\mathbf{x} \cdot \mathbf{V}_2^i) a_{2i}^u] \mathbf{V}_1^i + [a_{0i}^v + (\mathbf{x} \cdot \mathbf{V}_1^i) a_{1i}^v + (\mathbf{x} \cdot \mathbf{V}_2^i) a_{2i}^v] \mathbf{V}_2^i, \quad (5)$$

in which  $a_{0i}^u$  to  $a_{2i}^u$  and  $a_{0i}^v$  to  $a_{2i}^v$  are the unknown coefficients to be determined. Using that  $\mathbf{u}_i^l(\mathbf{x})$  is to be equal to the nodal value at node  $i$  gives

$$\begin{aligned} \bar{\mathbf{u}}_i &= \mathbf{u}_i^l(\bar{\mathbf{x}}_i) \\ &= [a_{0i}^u + (\bar{\mathbf{x}}_i \cdot \mathbf{V}_1^i) a_{1i}^u + (\bar{\mathbf{x}}_i \cdot \mathbf{V}_2^i) a_{2i}^u] \mathbf{V}_1^i + [a_{0i}^v + (\bar{\mathbf{x}}_i \cdot \mathbf{V}_1^i) a_{1i}^v + (\bar{\mathbf{x}}_i \cdot \mathbf{V}_2^i) a_{2i}^v] \mathbf{V}_2^i \end{aligned} \quad (6)$$

and hence

$$\mathbf{u}_i^l(\mathbf{x}) = \bar{\mathbf{u}}_i + \left( \xi_i \hat{u}_i^\xi + \eta_i \hat{u}_i^\eta \right) \mathbf{V}_1^i + \left( \xi_i \hat{v}_i^\xi + \eta_i \hat{v}_i^\eta \right) \mathbf{V}_2^i \quad (7a)$$

$$\text{with } \xi_i = (\mathbf{x} - \bar{\mathbf{x}}_i) \cdot \mathbf{V}_1^i, \quad \eta_i = (\mathbf{x} - \bar{\mathbf{x}}_i) \cdot \mathbf{V}_2^i, \quad \hat{u}_i^\xi = a_{1i}^u, \quad \hat{u}_i^\eta = a_{2i}^u, \quad \hat{v}_i^\xi = a_{1i}^v \quad \text{and} \quad \hat{v}_i^\eta = a_{2i}^v. \quad (7b)$$

In Eq. (7b), we note that, to improve the conditioning of the stiffness matrix, it is effective to scale the values  $\xi_i$  and  $\eta_i$  by the diameter of the largest finite element sharing the node  $i$ ,  $\tilde{h}_i$  [23,27,29]

$$\xi_i = (\mathbf{x} - \bar{\mathbf{x}}_i) \cdot \mathbf{V}_1^i / \tilde{h}_i, \quad \eta_i = (\mathbf{x} - \bar{\mathbf{x}}_i) \cdot \mathbf{V}_2^i / \tilde{h}_i. \quad (7c)$$

Substituting Eq. (7a) into Eq. (4), the displacement interpolation of the proposed shell element is obtained as

$$\begin{aligned} \mathbf{u}(r, s, t) = & \sum_{i=1}^3 h_i(r, s) \bar{\mathbf{u}}_i + \frac{t}{2} \sum_{i=1}^4 a_i f_i(r, s) (-\mathbf{V}_2^i \alpha_i + \mathbf{V}_1^i \beta_i) \\ & + \sum_{i=1}^3 h_i(r, s) \left[ (\xi_i \hat{u}_i^\xi + \eta_i \hat{u}_i^\eta) \mathbf{V}_1^i + (\xi_i \hat{v}_i^\xi + \eta_i \hat{v}_i^\eta) \mathbf{V}_2^i \right]. \end{aligned} \quad (8)$$

We note that in this local approximation, the difference to the development in Ref. [29] is that only the membrane displacements are enriched and hence less additional degrees of freedom are used at each node.

Finally, Eq. (8) can be rewritten as follows:

$$\mathbf{u}(r, s, t) = \bar{\mathbf{u}}(r, s, t) + \hat{\mathbf{u}}(r, s) \quad (9a)$$

with

$$\hat{\mathbf{u}}(r, s) = \sum_{i=1}^3 \mathbf{H}_i(r, s) \hat{\mathbf{u}}_i \quad \text{and} \quad \mathbf{H}_i(r, s) = h_i(r, s) \mathbf{V}_1^i [\xi_i \quad \eta_i \quad 0 \quad 0] + h_i(r, s) \mathbf{V}_2^i [0 \quad 0 \quad \xi_i \quad \eta_i], \quad (9b)$$

in which  $\hat{\mathbf{u}}_i = [\hat{u}_i^\xi \quad \hat{u}_i^\eta \quad \hat{v}_i^\xi \quad \hat{v}_i^\eta]^T$  and  $\mathbf{H}_i(r, s)$  are the vector of enriched nodal displacements for the membrane displacement of the shell element and the linear cover interpolation matrix for these displacements, respectively. Note that  $\bar{\mathbf{u}}_i$  is the vector of nodal displacements in the standard finite element procedure.

In the use of the above displacement interpolations, we need to suppress any linear dependence of the functions, and this is achieved by simply enforcing on the boundary with zero displacements not only  $\bar{\mathbf{u}}_i = 0$  but also  $\hat{u}_i^\xi = \hat{u}_i^\eta = \hat{v}_i^\xi = \hat{v}_i^\eta = 0$ , see Refs. [27–30].

## 2.2. Assumed covariant transverse shear strain fields

For linear analysis, the linear part of the Green–Lagrange strain tensor is used and its covariant strain components are

$$e_{ij} = \frac{1}{2} (\mathbf{u}_{,i} \cdot \bar{\mathbf{g}}_j + \bar{\mathbf{g}}_i \cdot \mathbf{u}_{,j}), \quad (10a)$$

in which

$$\bar{\mathbf{g}}_i = \frac{\partial \bar{\mathbf{x}}}{\partial r_i} \quad \text{and} \quad \mathbf{u}_{,i} = \frac{\partial \mathbf{u}}{\partial r_i} = \frac{\partial (\bar{\mathbf{u}} + \hat{\mathbf{u}})}{\partial r_i} = \bar{\mathbf{u}}_{,i} + \hat{\mathbf{u}}_{,i} \quad (10b)$$

$$\text{with } r_1 = r, \quad r_2 = s \quad \text{and} \quad r_3 = t. \quad (10c)$$

Then, the covariant strain components can be written in terms of Eq. (10b) as

$$e_{ij} = \bar{e}_{ij} + \hat{e}_{ij} \quad (11a)$$

$$\text{with } \bar{e}_{ij} = \frac{1}{2} (\bar{\mathbf{u}}_{,i} \cdot \bar{\mathbf{g}}_j + \bar{\mathbf{g}}_i \cdot \bar{\mathbf{u}}_{,j}) \quad \text{and} \quad \hat{e}_{ij} = \frac{1}{2} (\hat{\mathbf{u}}_{,i} \cdot \bar{\mathbf{g}}_j + \bar{\mathbf{g}}_i \cdot \hat{\mathbf{u}}_{,j}). \quad (11b)$$

While the in-plane covariant strain components are directly obtained in (11), the covariant transverse shear strains are assumed to alleviate transverse shear locking. Because the enriched displacement  $\hat{\mathbf{u}}$  is not affecting the transverse shear strains, the assumed transverse shear strain fields for the MITC3+ shell element can be directly adopted for the present element: [2]

$$\tilde{e}_{rt} = \frac{2}{3} \left( \bar{e}_{rt}^{(B)} - \frac{1}{2} \bar{e}_{st}^{(B)} \right) + \frac{1}{3} \left( \bar{e}_{rt}^{(C)} + \frac{1}{2} \bar{e}_{st}^{(C)} \right) + \frac{1}{3} \tilde{c} (3s - 1), \quad (12a)$$

$$\tilde{e}_{st} = \frac{2}{3} \left( \bar{e}_{st}^{(A)} - \frac{1}{2} \bar{e}_{rt}^{(A)} \right) + \frac{1}{3} \left( \bar{e}_{rt}^{(C)} + \frac{1}{2} \bar{e}_{st}^{(C)} \right) + \frac{1}{3} \tilde{c} (1 - 3r), \quad (12b)$$

where  $\tilde{c} = \bar{e}_{rt}^{(F)} - \bar{e}_{rt}^{(D)} - \bar{e}_{st}^{(F)} + \bar{e}_{st}^{(E)}$  and the tying positions (A), (B), (C), (D), (E), and (F) are presented in Fig. 3 and Table 1.

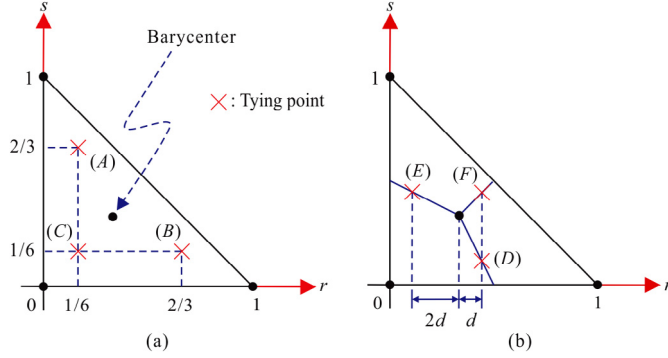


**Fig. 3.** Tying positions (A), (B), (C), (D), (E), and (F) for the assumed transverse shear strain fields for the present shell finite element.

**Table 1**

Tying positions for the assumed transverse shear strain of the present shell element. The distance  $d$  defined in Fig. 3(b), and  $d = 1/10,000$  is used [2,3].

	Tying position	$r$	$s$
Fig. 3(a)	(A)	1/6	2/3
	(B)	2/3	1/6
	(C)	1/6	1/6
Fig. 3(b)	(D)	1/3 + $d$	1/3 - 2 $d$
	(E)	1/3 - 2 $d$	1/3 + $d$
	(F)	1/3 + $d$	1/3 + $d$

### 3. Formulation for geometric nonlinear analysis

In this section, we extend the linear formulation presented in the previous section for geometric nonlinear analysis. We use the total Lagrangian formulation allowing for large displacements and large rotations [31]. In the formulation, a superscript (and subscript)  $t$  is used to denote “time” for general analysis, within static solutions “time” simply denoting the load step and configuration [6,31].

#### 3.1. Large displacement kinematics

The large displacement formulation of the element is achieved using the classical total Lagrangian formulation. Since the MITC procedure leads in linear analysis to an element formulation resembling the classical displacement formulation, except for internal strain assumptions, the nonlinear kinematics of the large displacement formulation can be directly established. Following this approach for shell analyses we have not observed an hourglass instability, like seen for example in Ref. [32], but a mathematical analysis would be valuable.

The geometry of the present shell element in the configuration at time  $t$  is shown in Fig. 1 and interpolated by

$${}^t\mathbf{x}(r, s, t) = {}^t\bar{\mathbf{x}}(r, s, t) + {}^t\hat{\mathbf{x}}(r, s) \quad (13a)$$

with

$${}^t\bar{\mathbf{x}}(r, s, t) = \sum_{i=1}^3 h_i(r, s) {}^t\bar{\mathbf{x}}_i + \frac{t}{2} \sum_{i=1}^4 a_i f_i(r, s) {}^t\mathbf{V}_n^i \quad \text{and} \quad (13b)$$

$${}^t\hat{\mathbf{x}}(r, s) = \sum_{i=1}^3 \mathbf{H}_i(r, s) {}^t\hat{\mathbf{x}}_i, \quad (13c)$$

in which  ${}^t\bar{\mathbf{x}}_i = [{}^t\bar{x}_i \ {}^t\bar{y}_i \ {}^t\bar{z}_i]^T$  is the standard position vector at node  $i$ ,  ${}^t\mathbf{V}_n^i = [{}^tV_{nx}^i \ {}^tV_{ny}^i \ {}^tV_{nz}^i]^T$  denotes the director vector at node  $i$ , and  ${}^t\hat{\mathbf{x}}_i = [{}^t\hat{x}_i^\xi \ {}^t\hat{x}_i^\eta \ {}^t\hat{y}_i^\xi \ {}^t\hat{y}_i^\eta]^T$  is the enriched position vector at node  $i$ . At time  $t = 0$ , the vector  $\hat{\mathbf{x}}_i$  is set to zero and it will be updated after calculating the incremental equilibrium equation.

The incremental displacements from the configuration at time  $t$  to the configuration at time  $t + \Delta t$  are given as

$$\mathbf{u}(r, s, t) = {}^{t+\Delta t}\mathbf{x}(r, s, t) - {}^t\mathbf{x}(r, s, t). \quad (14)$$

Using Eq. (13), Eq. (14) can be rewritten as

$$\mathbf{u}(r, s, t) = \bar{\mathbf{u}}(r, s, t) + \hat{\mathbf{u}}(r, s) \quad (15a)$$

with

$$\bar{\mathbf{u}}(r, s, t) = \sum_{i=1}^3 h_i(r, s) \bar{\mathbf{u}}_i + \frac{t}{2} \sum_{i=1}^4 a_i f_i(r, s) ({}^{t+\Delta t}\mathbf{V}_n^i - {}^t\mathbf{V}_n^i) \quad \text{and} \quad (15b)$$

$$\hat{\mathbf{u}}(r, s) = \sum_{i=1}^3 \mathbf{H}_i \hat{\mathbf{u}}_i, \quad (15c)$$

where  $\bar{\mathbf{u}}_i = [\bar{u}_i \ \bar{v}_i \ \bar{w}_i]^T$  and  $\hat{\mathbf{u}}_i = [\hat{u}_i^\xi \ \hat{u}_i^\eta \ \hat{v}_i^\xi \ \hat{v}_i^\eta]^T$  are the vector of incremental standard nodal displacements and the vector of incremental enriched nodal displacements at node  $i$  from time  $t$  to  $t + \Delta t$ , respectively. Note that  $\bar{\mathbf{u}}(r, s, t)$  and  $\hat{\mathbf{u}}(r, s)$  are the standard and enriched displacement vectors in the linear formulation, see Eqs. (3) and (9b).

The director vector at time  $t + \Delta t$  at node  $i$  is updated as follows [6]

$${}^{t+\Delta t}\mathbf{V}_n^i = {}^{t+\Delta t}_t\mathbf{Q} {}^t\mathbf{V}_n^i, \quad (16)$$

where  ${}^{t+\Delta t}_t\mathbf{Q}^i$  is the rotation matrix that rotates the director vector at node  $i$  from the configuration at time  $t$  to the configuration at time  $t + \Delta t$ . In addition, the two unit vectors  ${}^t\mathbf{V}_1^i$  and  ${}^t\mathbf{V}_2^i$  are obtained by (see Fig. 1(b))

$${}^t\mathbf{V}_1^i = \frac{\mathbf{e}_2 \times {}^t\mathbf{V}_n^i}{|\mathbf{e}_2 \times {}^t\mathbf{V}_n^i|} \quad \text{and} \quad {}^t\mathbf{V}_2^i = {}^t\mathbf{V}_n^i \times {}^t\mathbf{V}_1^i. \quad (17)$$

Note that for the special case  ${}^t\mathbf{V}_n^i$  parallel to  $\mathbf{e}_2$ , we simply use  ${}^t\mathbf{V}_1^i$  equal to  $\mathbf{e}_3$ .

For the vector-like parameterization of finite rotations, the following well-known formula is adopted

$${}^{t+\Delta t}_t\mathbf{Q}^i = \mathbf{I}_3 + \frac{\sin({}^{t+\Delta t}_t\theta^i)}{{}^{t+\Delta t}_t\theta^i} {}^{t+\Delta t}_t\boldsymbol{\Theta}^i + \frac{1}{2} \left[ \frac{\sin({}^{t+\Delta t}_t\theta^i/2)}{{}^{t+\Delta t}_t\theta^i/2} \right]^2 ({}^{t+\Delta t}_t\boldsymbol{\Theta}^i)^2 \quad (18a)$$

with

$${}^{t+\Delta t}_t\boldsymbol{\Theta}^i = \begin{bmatrix} 0 & -{}^{t+\Delta t}_t\theta_3^i & {}^{t+\Delta t}_t\theta_2^i \\ {}^{t+\Delta t}_t\theta_3^i & 0 & -{}^{t+\Delta t}_t\theta_1^i \\ -{}^{t+\Delta t}_t\theta_2^i & {}^{t+\Delta t}_t\theta_1^i & 0 \end{bmatrix}, \quad (18b)$$

$${}^{t+\Delta t}_t\boldsymbol{\theta}^i = \alpha_i {}^t\mathbf{V}_1^i + \beta_i {}^t\mathbf{V}_2^i, \quad (18c)$$

in which  $\mathbf{I}_3$  is a  $3 \times 3$  identity matrix,  ${}^{t+\Delta t}_t\boldsymbol{\Theta}^i$  is the skew-symmetric matrix operator,

$${}^{t+\Delta t}_t\boldsymbol{\theta}^i = [{}^{t+\Delta t}_t\theta_1^i \ {}^{t+\Delta t}_t\theta_2^i \ {}^{t+\Delta t}_t\theta_3^i]^T, \quad \text{and} \quad {}^{t+\Delta t}_t\theta_i = \sqrt{({}^{t+\Delta t}_t\theta_1^i)^2 + ({}^{t+\Delta t}_t\theta_2^i)^2 + ({}^{t+\Delta t}_t\theta_3^i)^2}. \quad (18d)$$

Using a Taylor series expansion, we have

$${}^{t+\Delta t}_t\mathbf{Q}^i = \mathbf{I}_3 + {}^{t+\Delta t}_t\boldsymbol{\Theta}^i + \frac{1}{2!} ({}^{t+\Delta t}_t\boldsymbol{\Theta}^i)^2 + \frac{1}{3!} ({}^{t+\Delta t}_t\boldsymbol{\Theta}^i)^3 + \dots \quad (19)$$

and keeping only the terms up to quadratic order, we obtain [6]

$${}^{t+\Delta t}\mathbf{V}_n^i - {}^t\mathbf{V}_n^i = {}^{t+\Delta t}_t\boldsymbol{\theta}^i \times {}^t\mathbf{V}_n^i + \frac{1}{2} {}^{t+\Delta t}_t\boldsymbol{\theta}^i \times ({}^{t+\Delta t}_t\boldsymbol{\theta}^i \times {}^t\mathbf{V}_n^i), \quad (20)$$

and the ‘consistent linearization’ including the quadratic terms

$${}^{t+\Delta t} \mathbf{V}_n^i - {}^t \mathbf{V}_n^i = -\alpha_i {}^t \mathbf{V}_2^i + \beta_i {}^t \mathbf{V}_1^i - \frac{1}{2} (\alpha_i^2 + \beta_i^2) {}^t \mathbf{V}_n^i. \quad (21)$$

Hence

$$\bar{\mathbf{u}}(r, s, t) = \sum_{i=1}^3 h_i(r, s) \bar{\mathbf{u}}_i + \frac{t}{2} \sum_{i=1}^4 a_i f_i(r, s) \left[ -\alpha_i {}^t \mathbf{V}_2^i + \beta_i {}^t \mathbf{V}_1^i - \frac{1}{2} (\alpha_i^2 + \beta_i^2) {}^t \mathbf{V}_n^i \right], \quad (22)$$

in which  $\alpha_i$  and  $\beta_i$  are the incremental rotations of the director vector  ${}^t \mathbf{V}_n^i$  about  ${}^t \mathbf{V}_1^i$  and  ${}^t \mathbf{V}_2^i$ , respectively, at node  $i$ .

The vector of incremental standard displacements,  $\bar{\mathbf{u}}$  can now be considered to consist of two parts, a linear part  $\bar{\mathbf{u}}_l$  and a quadratic part  $\bar{\mathbf{u}}_q$  as follows

$$\bar{\mathbf{u}}(r, s, t) = \bar{\mathbf{u}}_l(r, s, t) + \bar{\mathbf{u}}_q(r, s, t) \quad (23a)$$

with

$$\bar{\mathbf{u}}_l(r, s, t) = \sum_{i=1}^3 h_i(r, s) \bar{\mathbf{u}}_i + \frac{t}{2} \sum_{i=1}^4 a_i f_i(r, s) (-\alpha_i {}^t \mathbf{V}_2^i + \beta_i {}^t \mathbf{V}_1^i) \text{ and} \quad (23b)$$

$$\bar{\mathbf{u}}_q(r, s, t) = -\frac{t}{4} \sum_{i=1}^4 a_i f_i(r, s) [(\alpha_i^2 + \beta_i^2) {}^t \mathbf{V}_n^i]. \quad (23c)$$

### 3.2. Green–Lagrange strains

The covariant components of the Green–Lagrange strain tensor in the configuration at time  $t$ , referred to the configuration at time 0, are given by [6]

$${}^t \varepsilon_{ij} = \frac{1}{2} ({}^t \mathbf{g}_i \cdot {}^t \mathbf{g}_j - {}^0 \mathbf{g}_i \cdot {}^0 \mathbf{g}_j) \quad (24a)$$

$$\text{with } {}^0 \mathbf{g}_i = \frac{\partial {}^0 \bar{\mathbf{x}}}{\partial r_i}, \quad {}^t \mathbf{g}_i = \frac{\partial ({}^t \bar{\mathbf{x}} + {}^t \hat{\mathbf{x}})}{\partial r_i} = {}^t \bar{\mathbf{g}}_i + {}^t \bar{\mathbf{u}}_{,i} + {}^t \hat{\mathbf{u}}_{,i}, \quad (24b)$$

$${}^t \bar{\mathbf{u}}_{,i} = \frac{\partial {}^t \bar{\mathbf{u}}}{\partial r_i}, \quad {}^t \hat{\mathbf{u}}_{,i} = \frac{\partial {}^t \hat{\mathbf{u}}}{\partial r_i}, \quad {}^t \bar{\mathbf{u}} = {}^t \bar{\mathbf{x}} - {}^0 \bar{\mathbf{x}}, \quad {}^t \hat{\mathbf{u}} = {}^t \hat{\mathbf{x}}, \quad r_1 = r, \quad r_2 = s, \quad r_3 = t. \quad (24c)$$

Then, the incremental covariant components of the strain are

$${}^0 \varepsilon_{ij} = {}^{t+\Delta t} {}^0 \varepsilon_{ij} - {}^t \varepsilon_{ij} = \frac{1}{2} ({}^0 \mathbf{u}_{,i} \cdot {}^t \mathbf{g}_j + {}^t \mathbf{g}_i \cdot {}^0 \mathbf{u}_{,j} + {}^0 \mathbf{u}_{,i} \cdot {}^0 \mathbf{u}_{,j}) \quad \text{with } {}^0 \mathbf{u}_{,i} = \frac{\partial (\bar{\mathbf{u}} + \hat{\mathbf{u}})}{\partial r_i}. \quad (25)$$

Using Eq. (24) in Eq. (25) and retaining only the strain terms up to the second order of unknowns, the incremental strain components are approximated as

$${}^0 e_{ij} \approx {}^0 \varepsilon_{ij} + {}^0 \eta_{ij}, \quad (26a)$$

where  ${}^0 e_{ij}$  and  ${}^0 \eta_{ij}$  are linear and nonlinear parts, respectively,

$${}^0 e_{ij} = \frac{1}{2} \left( \frac{\partial (\bar{\mathbf{u}}_l + \hat{\mathbf{u}})}{\partial r_i} \cdot ({}^t \bar{\mathbf{g}}_j + {}^t \hat{\mathbf{g}}_j) + ({}^t \bar{\mathbf{g}}_i + {}^t \hat{\mathbf{g}}_i) \cdot \frac{\partial (\bar{\mathbf{u}}_l + \hat{\mathbf{u}})}{\partial r_j} \right) = {}^0 \mathbf{B}_{ij} \mathbf{U}, \quad (26b)$$

$${}^0 \eta_{ij} = \frac{1}{2} \left( \frac{\partial (\bar{\mathbf{u}}_l + \hat{\mathbf{u}})}{\partial r_i} \cdot \frac{\partial (\bar{\mathbf{u}}_l + \hat{\mathbf{u}})}{\partial r_j} \right) + \frac{1}{2} \left( \frac{\partial \bar{\mathbf{u}}_q}{\partial r_i} \cdot ({}^t \bar{\mathbf{g}}_j + {}^t \hat{\mathbf{g}}_j) + ({}^t \bar{\mathbf{g}}_i + {}^t \hat{\mathbf{g}}_i) \cdot \frac{\partial \bar{\mathbf{u}}_q}{\partial r_j} \right) = \frac{1}{2} \mathbf{U}^T {}^0 \mathbf{N}_{ij} \mathbf{U}, \quad (26c)$$

in which  ${}^0 \mathbf{B}_{ij}$  and  ${}^0 \mathbf{N}_{ij}$  are linear and nonlinear strain–displacement matrices, respectively.  $\mathbf{U}$  is the degrees of freedom vector including incremental standard nodal displacements  $\bar{\mathbf{u}}_i$ ,  $\alpha_i$ , and  $\beta_i$ , and incremental enriched nodal displacements  $\hat{\mathbf{u}}_i$  for all element nodes. In addition, the strain variations are

$$\delta {}^0 e_{ij} = {}^0 \mathbf{B}_{ij} \delta \mathbf{U} \quad \text{and} \quad \delta {}^0 \eta_{ij} = \delta \mathbf{U}^T {}^0 \mathbf{N}_{ij} \mathbf{U}. \quad (27)$$

To reduce transverse shear locking, the assumed strain fields are employed as in the linear formulation, but are applied to the incremental covariant transverse shear strains. We can rewrite the covariant components of the incremental Green–Lagrange strain tensor for the transverse shear strain field as

$${}_0\varepsilon_{it} \approx {}_0e_{it} + {}_0\eta_{it} \quad (28a)$$

with

$${}_0e_{it} = \frac{1}{2} \left( \frac{\partial \bar{\mathbf{u}}_l}{\partial r_i} \cdot ({}^t\bar{\mathbf{g}}_3 + {}^t\hat{\mathbf{g}}_3) + ({}^t\bar{\mathbf{g}}_i + {}^t\hat{\mathbf{g}}_i) \cdot \frac{\partial \bar{\mathbf{u}}_l}{\partial r_3} \right), \quad (28b)$$

$${}_0\eta_{it} = \frac{1}{2} \left( \frac{\partial \bar{\mathbf{u}}_l}{\partial r_i} \cdot \frac{\partial \bar{\mathbf{u}}_l}{\partial r_3} \right) + \frac{1}{2} \left( \frac{\partial \bar{\mathbf{u}}_q}{\partial r_i} \cdot ({}^t\bar{\mathbf{g}}_3 + {}^t\hat{\mathbf{g}}_3) + ({}^t\bar{\mathbf{g}}_i + {}^t\hat{\mathbf{g}}_i) \cdot \frac{\partial \bar{\mathbf{u}}_q}{\partial r_3} \right), \quad (28c)$$

and  $r_1 = r$ ,  $r_2 = s$ ,  $r_3 = t$ .

The assumed covariant transverse shear strains using (28) are calculated by

$${}_0\tilde{\varepsilon}_{rt} = \frac{2}{3} \left( {}_0\varepsilon_{rt}^B - \frac{1}{2} {}_0\varepsilon_{st}^B \right) + \frac{1}{3} ({}_0\varepsilon_{rt}^C + {}_0\varepsilon_{st}^C) + \frac{1}{3} {}_0\tilde{c} (3s - 1), \quad (29a)$$

$${}_0\tilde{\varepsilon}_{st} = \frac{2}{3} \left( {}_0\varepsilon_{st}^A - \frac{1}{2} {}_0\varepsilon_{rt}^A \right) + \frac{1}{3} ({}_0\varepsilon_{rt}^C + {}_0\varepsilon_{st}^C) + \frac{1}{3} {}_0\tilde{c} (1 - 3r), \quad (29b)$$

$${}_0\tilde{\varepsilon}_{it} = {}_0\tilde{\varepsilon}_{it} + {}_0\tilde{\eta}_{it}, \quad {}_0\tilde{\varepsilon}_{it} = {}_0\mathbf{B}_{it}\mathbf{U}, \quad {}_0\tilde{\eta}_{it} = \frac{1}{2} \mathbf{U}^T {}_0\mathbf{N}_{it} \mathbf{U}, \quad (29c)$$

in which  ${}_0\tilde{c} = {}_0\varepsilon_{rt}^F - {}_0\varepsilon_{rt}^D - {}_0\varepsilon_{st}^F + {}_0\varepsilon_{st}^E$  and  ${}_0\mathbf{B}_{it}$  and  ${}_0\mathbf{N}_{it}$  are the strain–displacement matrices for the assumed covariant transverse shear strains. Of course, the tying positions defined in Fig. 3 and Table 1 are used.

### 3.3. Stiffness matrix and internal force vector

In the total Lagrangian formulation, the tangent stiffness matrix ( ${}^t_0\mathbf{K}_e$ ) and internal force vector ( ${}^t_0\mathbf{F}_e$ ) of the shell element are [6]

$${}^t_0\mathbf{K}_e = \int_{^0V} {}^t_0\mathbf{B}_{ij}^T {}^t_0C_{ijkl} {}^t_0\mathbf{B}_{kl} d^0V + \int_{^0V} {}^t_0S^{ij} {}^t_0\mathbf{N}_{ij} d^0V, \quad (30a)$$

$${}^t_0\mathbf{F}_e = \int_{^0V} {}^t_0\mathbf{B}_{ij}^T {}^t_0S_{ij} d^0V, \quad (30b)$$

where  ${}^0V$  is the volume of the shell element in the configuration at time 0,  ${}_0\mathbf{B}_{ij}$  and  ${}_0\mathbf{N}_{ij}$  are the linear and nonlinear strain–displacement matrices including the initial displacement effect, and  ${}_0C^{ijkl}$  and  ${}_0S^{ij}$  denote the material law tensor and the second Piola–Kirchhoff stress, respectively.

For the evaluation of the element stiffness matrix and internal nodal force vector, we use 7-point Gauss integration in the  $r$ – $s$  plane due to, both, the cubic bubble function used for the rotations and the enrichment of the membrane displacements, and 2-point Gauss integration through the element thickness. The degrees of freedom corresponding to the bubble function can be condensed out at the element level for computational efficiency. With the full Newton–Raphson iteration scheme, the stiffness matrix can be updated at each iteration; thereby obtaining a quadratic rate of solution convergence.

## 4. Numerical examples

The present shell element passes the basic tests, namely, the isotropy, zero energy mode and patch tests. Furthermore, the shell element shows excellent convergence behavior in both membrane and bending dominated shell problems, even when distorted meshes are applied. To show the performance of the present shell element, several linear and nonlinear benchmark problems are solved in this section. A list of finite elements used for comparison with the proposed shell element is given in Table 2. Since we want to compare with the solutions given in earlier published papers, we simply use point values of the solutions and not a norm as would be more appropriate in a thorough element evaluation [6,9,18].

**Table 2**

List of finite elements used for comparison.

Element	Description	Ref.
Triangular elements	MITC3+	[2,3]
	ALL88	[21]
	ANDES	[21]
	ES-ANDES	[16]
	ANS6S	[33]
	DSG3	[34]
Quadrilateral elements	CS-DSG3	[17]
	MITC4	[13]
	MITC4+	[18]
	MITC4*	[13,20]
	MITC9	[35]
	Q6	[19]
Quadrilateral elements	QM6	[19]
	P-S	[36]
	PEAS7	[11]
	SIMO	[37]
	QPH	[38]
	QUAD4	[39]
URI-9	URI-9	[40]

In each example, the reference solutions are given by either analytical solutions or solutions obtained using a fine uniform mesh of MITC9 shell elements [35]. The 9-node MITC9 shell element is known to satisfy the ellipticity and consistency conditions and to show reliable convergence behaviors. Also, by imposing  $w = \alpha = \beta = 0$  for all nodes, plane stress problems modeled in the  $x-y$  plane are solved in some benchmark problems to evaluate the membrane behavior. As expected, the MITC3+ element does not perform well in such solutions because in these cases, the results are simply those obtained using the 3-node constant strain triangular element.

In the discretizations considered below, we refer to the meshes used with quadrilateral elements and imply the use of two triangular elements for each quadrilateral element.

#### 4.1. Linear benchmark problems

Four popular benchmark problems for linear analysis are considered here to demonstrate the performance of the proposed element.

##### 4.1.1. Skew beam

The skew beam problem proposed by Cook [41] is useful to assess the membrane performance of finite elements. The geometric dimensions and boundary conditions used are shown in Fig. 4(a). The skew beam is subjected to a distributed shear load  $p = 1/16$  per unit length at the right end. Plane stress conditions are used and the material properties are Young's modulus  $E = 1.0$  and Poisson's ratio  $\nu = 1/3$ . The reference solution of the vertical displacement at the free-end mid-point A is 23.95 given in Ref. [41]. The solutions are obtained using  $N \times N$  element meshes ( $N = 2, 4, 8$ , and 16) and thus using  $2 \times N \times N$  triangular elements. Two different mesh patterns, shown in Fig. 4(b), are considered for the triangular elements. The deflections at point A were computed and are listed in Table 3 along with the results using other elements. The excellent performance of the present element can be observed.

##### 4.1.2. Cantilever beam

The thin cantilever beam suggested by MacNeal [42] has frequently been used as a test problem. The cantilever beam has length  $L = 6$ , width  $B = 0.2$ , and thickness  $h = 0.1$ . The material properties are given by Young's modulus

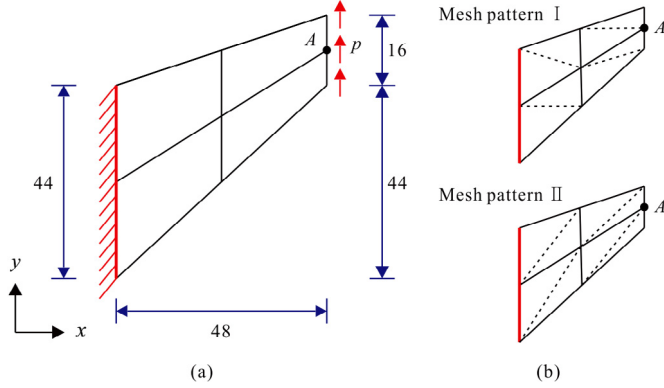


**Fig. 4.** Cook's skew beam: (a) Problem description, (b) Mesh patterns ( $2 \times 2$ ) used for the triangular elements.

**Table 3**

Normalized vertical displacement at point A for the Cook's skew beam shown in Fig. 4(a).

Element type		Mesh			
		$2 \times 2$	$4 \times 4$	$8 \times 8$	$16 \times 16$
Triangular element	MITC3+, mesh I	0.50	0.76	0.92	0.98
	MITC3+, mesh II	0.28	0.47	0.72	0.90
	ALL88, mesh I	0.80	0.91	0.98	1.00
	ANDES, mesh I	0.86	0.94	0.98	0.99
	ES-ANDES, mesh I	0.79	0.96	0.99	1.00
	Present, mesh I	0.95	0.99	1.00	1.00
	Present, mesh II	0.84	0.96	0.99	1.00
Quadrilateral element	MITC4	0.49	0.76	0.92	0.98
	MITC4*	0.88	0.96	0.99	1.00
	MITC4+	0.73	0.91	0.98	0.99
	Q6	0.96	0.98	1.00	1.00
	QM6	0.88	0.96	0.99	1.00

Reference solution  $v_{ref}$  [41] = 23.9

Mesh patterns I and II are shown in Fig. 4(b)

$E = 10^7$  and Poisson's ratio  $\nu = 0.3$ . We consider two loading cases: a shearing force ( $P = 1$ ) and a moment ( $M = 0.2$ ) at the free tip.

We use three different meshes (with rectangular, parallelogram, and trapezoidal 4-node element shapes), as shown in Fig. 5(a). In addition, two triangular mesh patterns (shown in Fig. 5(b)) are used for the triangular elements. Tables 4 and 5 give the tip displacements at point A ( $v_A$ ) calculated using the reference value of  $v_{ref} = -0.1081$  for the shearing load case and  $v_{ref} = -0.0054$  for the moment load case [42]. The results for the present element are compared with those obtained for previously developed elements. The present shell element shows high accuracy in all cases regardless of mesh distortions.

#### 4.1.3. Hemispherical shell

We consider a hemispherical shell with an  $18^\circ$  hole at the top (Fig. 6). The hemispherical shell has the radius  $r = 10$ , thickness  $h = 0.04$ , Young's modulus  $E = 6.825 \times 10^7$ , and Poisson's ratio  $\nu = 0.3$ . Due to symmetry, only one quarter of the shell is modeled and two mesh patterns (I and II; shown in Fig. 6) are used for the triangular elements. We consider not only meshes that are uniform but also distorted meshes, as shown in Fig. 7. When the  $N \times N$  element distorted mesh is used, each edge is divided by the ratio  $L_1:L_2:L_3:\dots:L_N = 1:2:3\dots:N$ , leading to severely distorted meshes.

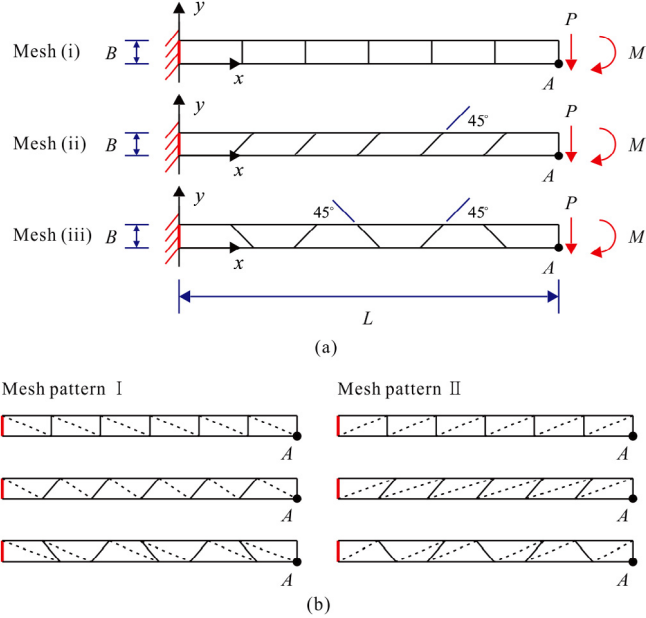


**Fig. 5.** Cantilever beam subjected to two different loadings: Unit tip shear force  $P$  and unit tip bending moment  $M$ . (a) Problem description, (b) Mesh patterns ( $1 \times 6$ ) used for triangular elements.

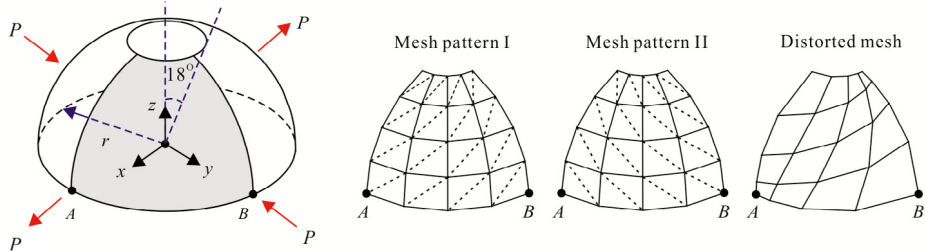


**Fig. 6.** Problem description of the hemispherical shell with an  $18^\circ$  hole. Mesh patterns I and II for the triangular elements and distorted meshes used.

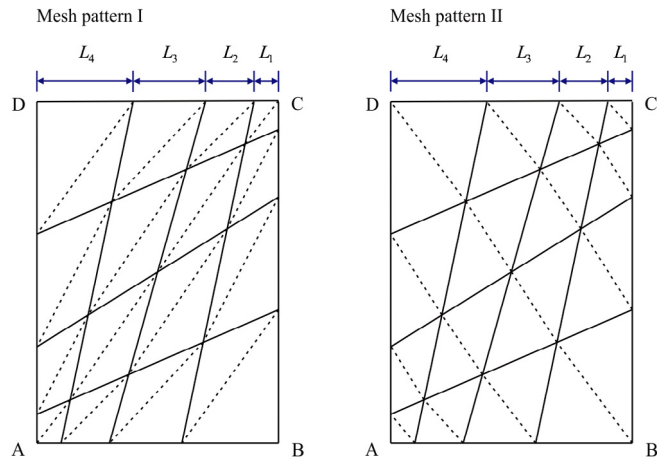


**Fig. 7.** Distorted mesh patterns used for the problems considered when solved with  $N = 4$ .

**Table 4**

Normalized vertical displacement at point A,  $v_A$  for the MacNeal's cantilever beam subjected to unit tip shear force,  $P = 1$ .

Element type		Load $P$		
		Mesh (i)	Mesh (ii)	Mesh (iii)
Triangular element	MITC3+, mesh I	0.0315	0.0222	0.0148
	MITC3+, mesh II	0.0315	0.0111	0.0194
	Present, mesh I	0.9833	0.9704	0.9611
	Present, mesh II	0.9833	0.9519	0.9639
Quadrilateral element	MITC4	0.0934	0.0342	0.0268
	MITC4*	0.9926	0.6318	0.0518
	MITC4+	0.9038	0.1730	0.0435
	Q6	0.9926	0.6772	0.1064
	QM6	0.9926	0.6226	0.0444
	P-S	0.9926	0.7983	0.2211
	PEAS7	0.9824	0.7946	0.2174

Reference solution  $v_{ref}$  [42] = -0.1081

Mesh patterns I and II are shown in Fig. 5(b)

**Table 5**

Normalized displacement at point A,  $v_A$  for the MacNeal's cantilever beam subjected to tip moment,  $M = 0.2$ .

Element type		Load $M$		
		Mesh (i)	Mesh (ii)	Mesh (iii)
Triangular element	MITC3+, mesh I	0.0370	0.0185	0.0185
	MITC3+, mesh II	0.0370	0.0185	0.0185
	Present, mesh I	1.0000	1.0000	1.0000
	Present, mesh II	1.0000	1.0000	1.0000
Quadrilateral element	MITC4	0.0926	0.0370	0.0185
	MITC4*	1.0000	0.7222	0.0556
	MITC4+	0.9074	0.1852	0.0370
	Q6	1.0000	0.7593	0.0926
	QM6	1.0000	0.7222	0.0370
	P-S	1.0000	0.8519	0.1667

Reference solution  $v_{ref}$  [42] = -0.0054

Mesh patterns I and II are shown in Fig. 5(b)

The shell is subjected to two pairs of opposite radial concentrated loads  $P = 2$ . This problem is useful for evaluating the ability of the element to represent rigid-body rotations and inextensible bending modes. The reference value for the radial displacement at the load point is  $u_{ref} = 0.094$  [42].

Table 6 gives the radial displacement of the present element compared with results obtained using different shell elements, and Fig. 8(a) shows the normalized displacements with respect to the reference solution when the uniform and distorted meshes are adopted. The solution using the MITC4 shell element significantly deteriorates due to the effect of mesh distortions, even when using incompatible modes (used in the MITC4\* element [13,20]). It can be observed that the results of the MITC3+, MITC4+ and present element agree well with the reference solution.

#### 4.1.4. Scordelis–Lo roof

The Scordelis–Lo roof problem is a classical benchmark problem to assess the performance of shell elements. An asymptotically mixed bending–membrane behavior is observed [43]. The roof structure shown in Fig. 9(a) is supported by rigid diaphragms at its curved edges while the straight edges are free. The radius of curvature is  $R = 25$  and the length and thickness of the roof are  $L = 50$  and  $h = 0.25$ , respectively. The material has Young's modulus  $E = 4.32 \times 10^8$  and Poisson's ratio  $\nu = 0$ . The roof is loaded by its own weight, to a uniform vertical gravity load of  $f_z = 90$  per unit area.

**Table 6**

Normalized radial displacement at point A for the hemispherical shell with an 18° hole shown in Fig. 6 when uniform meshes are used.

	Element type	Mesh		
		4 × 4	8 × 8	16 × 16
Triangular elements	MITC3+, mesh I	1.0277	0.9936	0.9851
	MITC3+, mesh II	1.0000	0.9862	0.9830
	ANS6S, mesh I	0.9489	0.9819	1.0011
	DSG3, mesh I	0.9649	0.9809	0.9894
	CS-DSG3, mesh I	1.0098	1.0028	1.0007
	Present, mesh I	1.0106	0.9894	0.9894
	Present, mesh II	0.9787	0.9894	0.9894
Quadrilateral elements	MITC4	1.0330	0.9957	0.9904
	MITC4*	1.0330	0.9979	0.9926
	MITC4+	1.0330	0.9979	0.9926
	SIMO	1.0043	0.9979	0.9989

Reference solution  $u_{ref}$  [42] = 0.094

Mesh patterns I and II are shown in Fig. 6

**Table 7**

Normalized displacement at the point A for the Scordelis–Lo roof shown in Fig. 9(a) when uniform meshes are used.

	Element type	Mesh		
		4 × 4	8 × 8	16 × 16
Triangular element	MITC3+, mesh I	0.7312	0.8743	0.9593
	MITC3+, mesh II	0.6677	0.8558	0.9540
	CS-DSG3	0.7278	0.9015	1.0043
	Present, mesh I	0.9610	0.9931	0.9983
	Present, mesh II	0.8922	0.9762	0.9950
Quadrilateral element	MITC4	0.9431	0.9729	0.9888
	MITC4*	1.0473	1.0053	0.9977
	MITC4+	1.0476	1.0053	0.9977
	QPH	0.9401	0.9802	1.0099
	SIMO	1.0830	1.0149	1.0000
	QUAD4	1.0499	1.0079	–
	URI-9	1.2189	1.0539	1.0169

Reference solution  $w_{ref}$  [42] = −0.3024

Mesh patterns I and II are shown in Fig. 9(b)

Due to symmetry, only one quarter of the shell is modeled and the two mesh patterns shown in Fig. 9(b) are considered for triangular shell elements. The widely adopted reference solution for the vertical deflection at the center of the free edge (point A) is  $w_{ref} = -0.3024$  [38]. Normalized displacements are plotted in Fig. 10 and are compared with those of other elements listed in Table 7. The present shell element exhibits still good results even though the distorted meshes are used.

#### 4.2. Nonlinear test problems

In this section, the performance of the present shell element is evaluated in the geometric nonlinear range. The Newton–Raphson iterations to solve the nonlinear equations are performed in each load step to a convergence tolerance of 0.1 percent of the relative incremental energy [6].

##### 4.2.1. Cantilever beam subjected to a tip moment

A cantilever beam subjected to a tip moment  $M = 10\pi$  is considered as shown in Fig. 11(a). The length, depth, and thickness of the beam are  $L = 20$ ,  $B = 1$ , and  $h = 1$ , respectively. Young's modulus and Poisson's ratio are  $E = 1,200$  and  $\nu = 0.2$ . The tip moment is sufficient to roll up the cantilever beam into a circular ring.

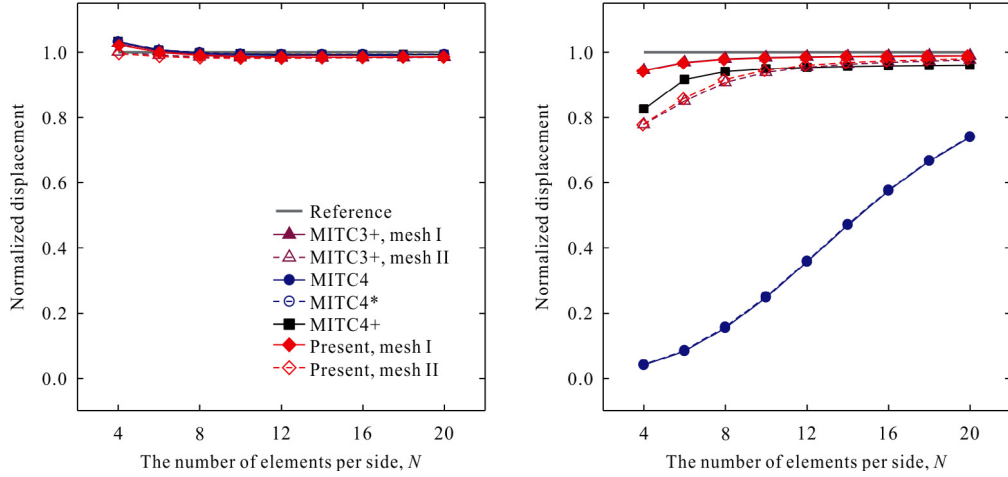


**Fig. 8.** Normalized displacement for the hemispherical shell with an  $18^\circ$  hole using uniform (left) and distorted meshes (right).

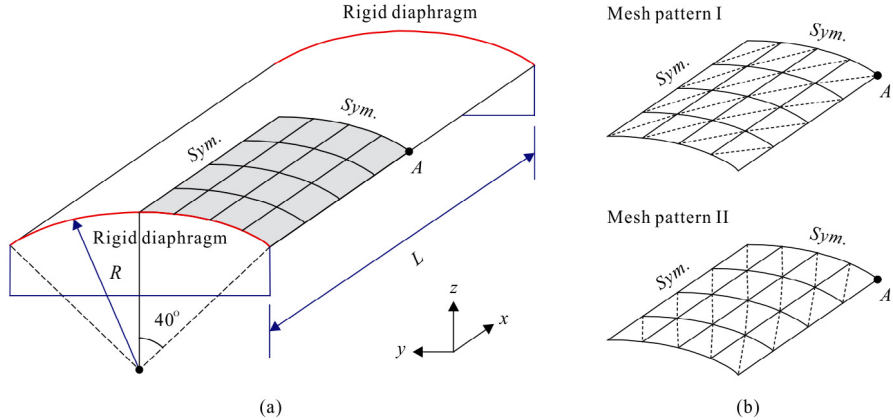


**Fig. 9.** Scordelis–Lo roof: (a) Problem description, (b) Mesh patterns I and II ( $4 \times 4$ ) used for the triangular shell elements.

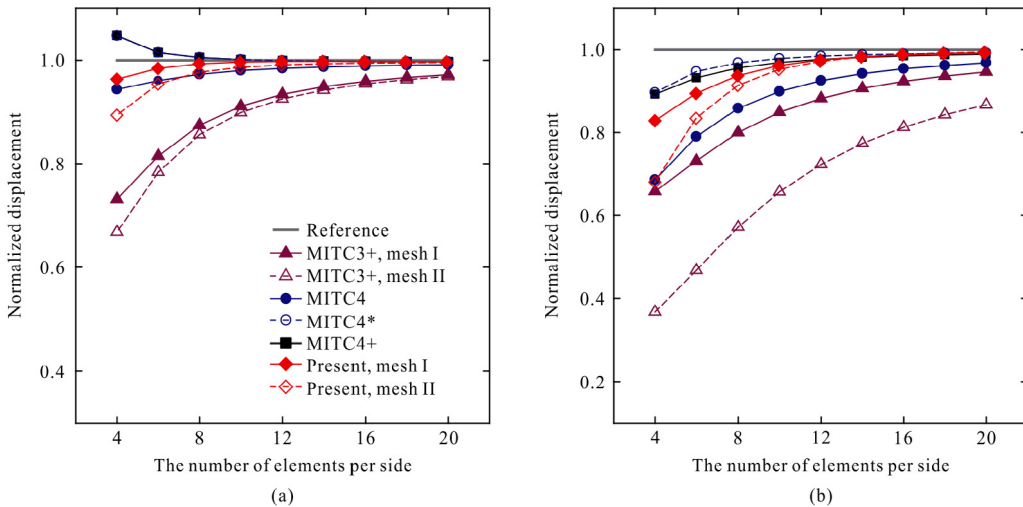


**Fig. 10.** Normalized displacement calculated for the Scordelis–Lo roof with (a) uniform and (b) distorted meshes shown in Fig. 7.

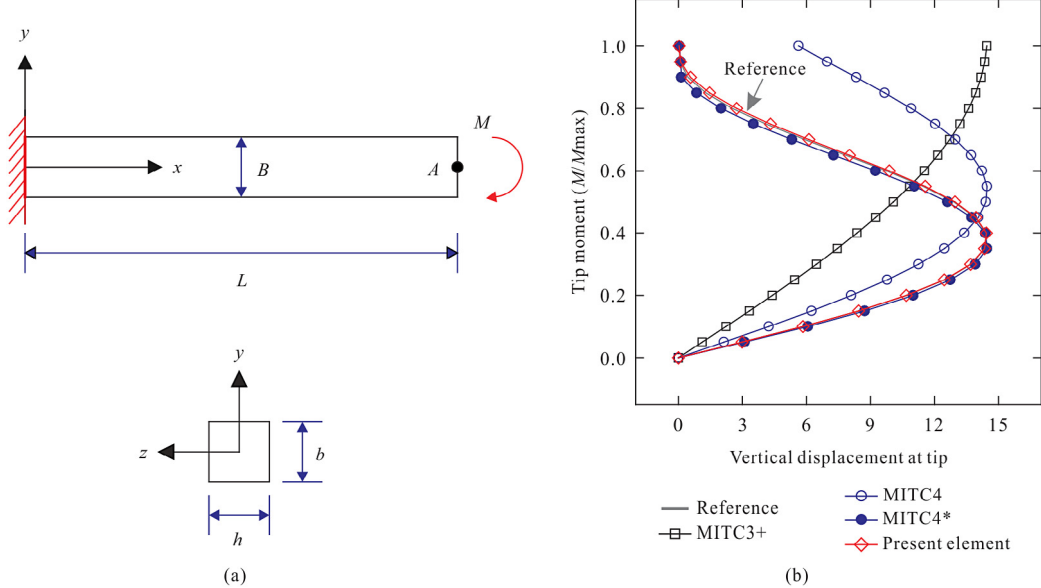


**Fig. 11.** Cantilever beam subjected to a tip moment: (a) Problem description, (b) Load–displacement curve for the cantilever beam.

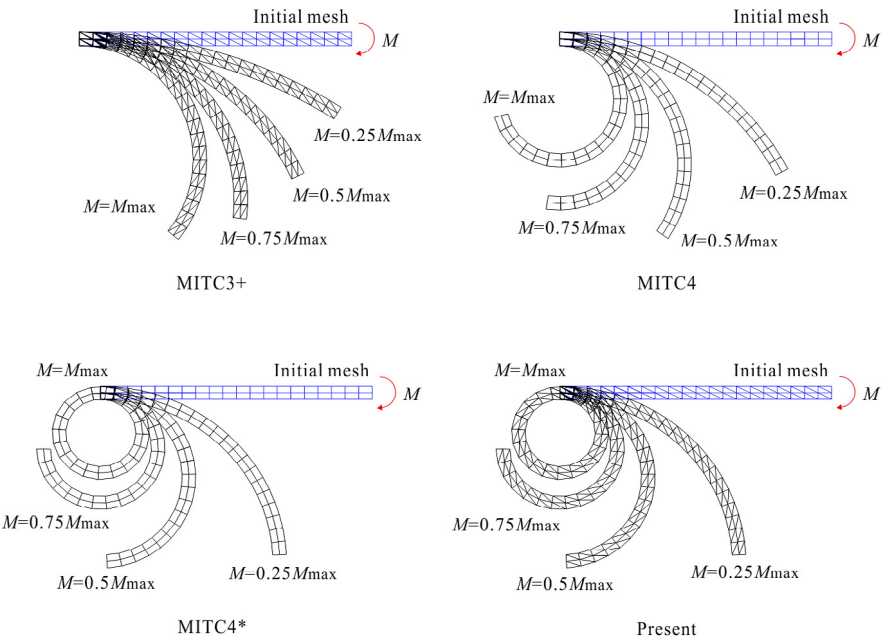


**Fig. 12.** Predicted deformed configurations for the cantilever beam subjected to a tip moment.

This cantilever beam is modeled using a  $20 \times 2$  element mesh and the mesh pattern used for the triangular shell elements is depicted in Fig. 12. Fig. 11(b) presents the load–displacement curve for point  $A$  and Fig. 12 shows the final deformed shapes calculated using the MITC3+, MITC4, MITC4\*, and present shell elements. The present and MITC4\* elements provide much better performance than do the other elements, and the results compare favorably with the reference solution.

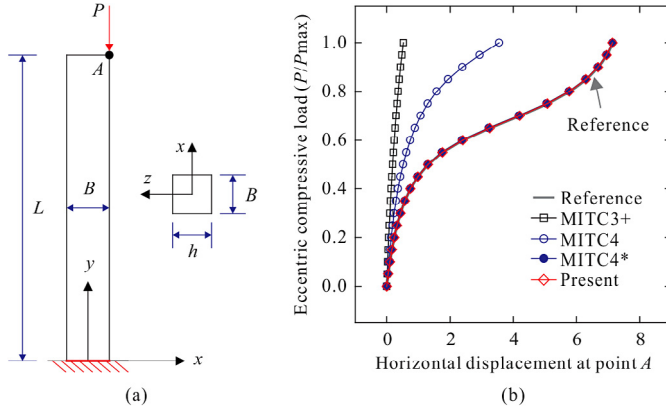


**Fig. 13.** Column under an eccentric compressive load: (a) Problem description, (b) Predicted load–displacement curves for the column.

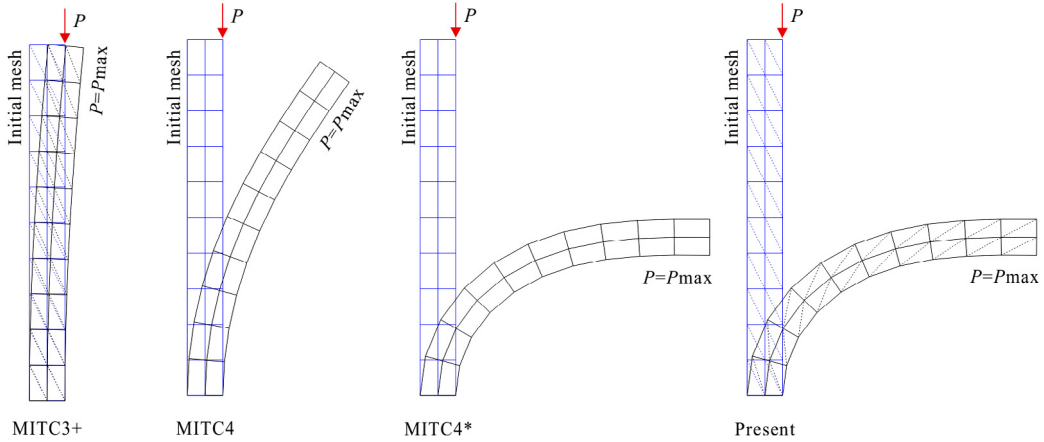


**Fig. 14.** Calculated deformed configurations for the column under an eccentric compressive load.

#### 4.2.2. Column under an eccentric compressive load

A column is subjected to an eccentric compressive load as shown in Fig. 13(a). The length, width, and thickness of the column are  $L = 10$ ,  $B = 1$ , and  $h = 1$ , respectively. Young's modulus and Poisson's ratio are taken as  $E = 10^6$  and  $\nu = 0$ , respectively.

The geometry is meshed with  $2 \times 10$  elements as shown in Fig. 14. The reference solution is obtained using a  $4 \times 20$  uniform mesh of MITC9 shell elements. The horizontal deflection at point A of the column and the corresponding load–deflection curves are plotted in Fig. 13(b). The deflections given by the MITC4\* and present elements agree very well with the deflection of the reference solution. The final deformed configurations obtained using the MITC3+, MITC4, MITC4\*, and present elements are shown in Fig. 14.

#### 4.2.3. Hemispherical shells

We consider again the hemispherical shell problem and now to assess the geometric nonlinear performance of the present element. The material and geometrical properties are as used in the linear analysis (see Section 4.1.3). One quarter of each hemispherical shell is considered by employing symmetry conditions. Two triangular mesh patterns (I and II; shown in Fig. 6) are also considered for the triangular elements.

Two pairs of opposite radial concentrated loads at the bottom edge of the shell are incrementally applied to the maximum value  $P_{\max} = 400$ . The shell is modeled using a  $6 \times 6$  element mesh with uniform and distorted patterns. The reference solution are obtained using a  $16 \times 16$  element mesh of MITC9 shell elements. The load–radial

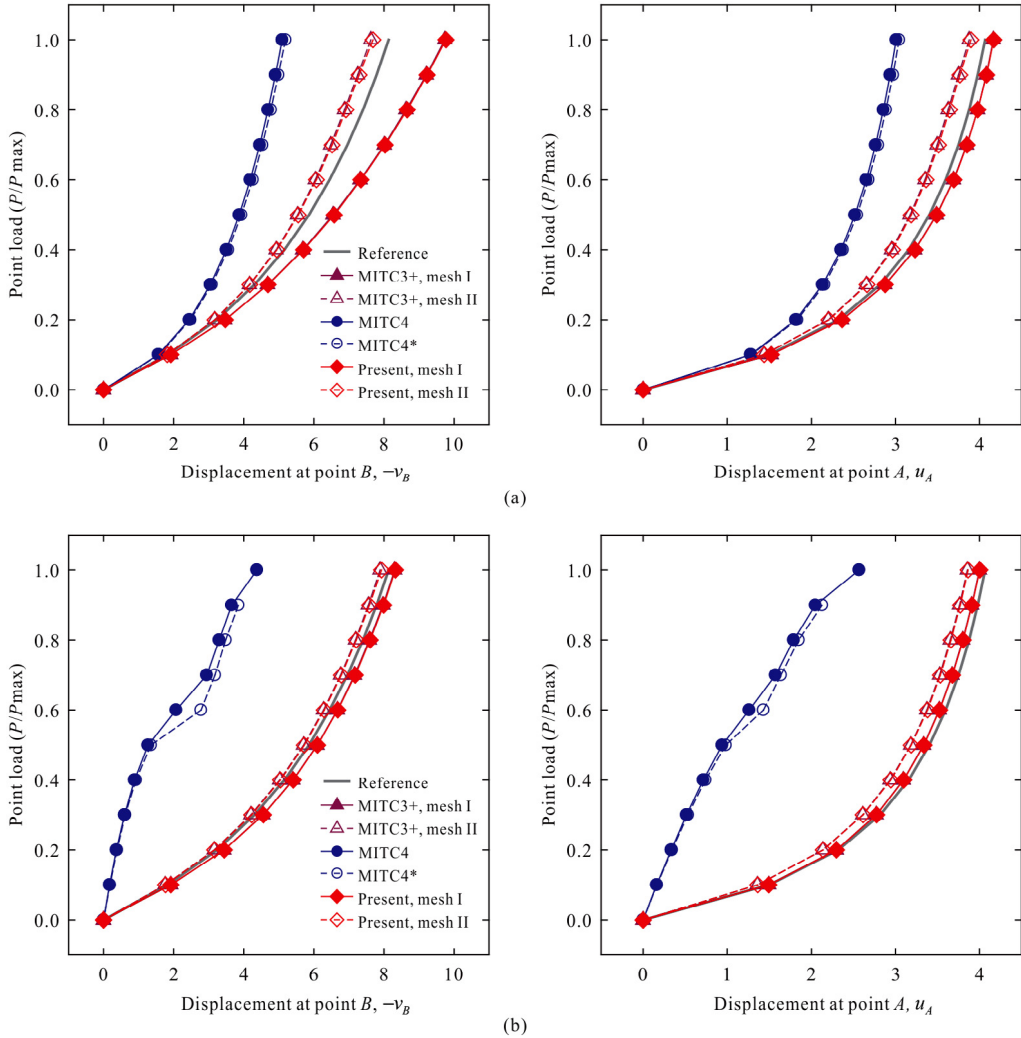


**Fig. 15.** Calculated load–displacement curves for the hemispherical shell with an  $18^\circ$  hole when used in (a) uniform and (b) distorted meshes.

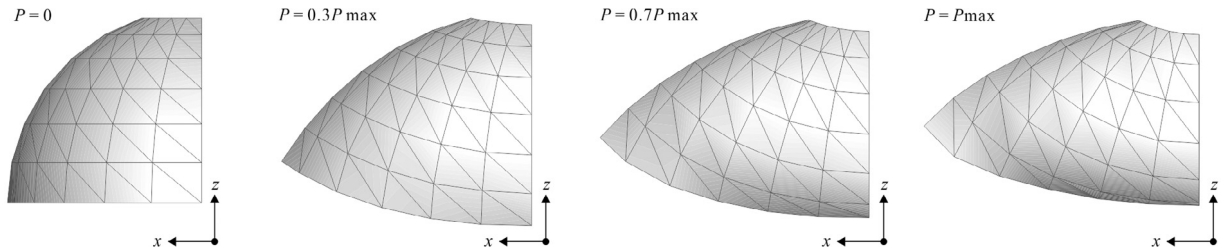


**Fig. 16.** Predicted deformed configurations for the hemispherical shell with an  $18^\circ$  hole.

displacement curves at two different points,  $A$  and  $B$ , are displayed in Fig. 15. The curves show that the MITC3+ and present shell elements exhibit excellent behavior when either uniform or distorted meshes are used. The deformed shapes obtained using a  $6 \times 6$  element mesh of the present element are shown in Fig. 16.

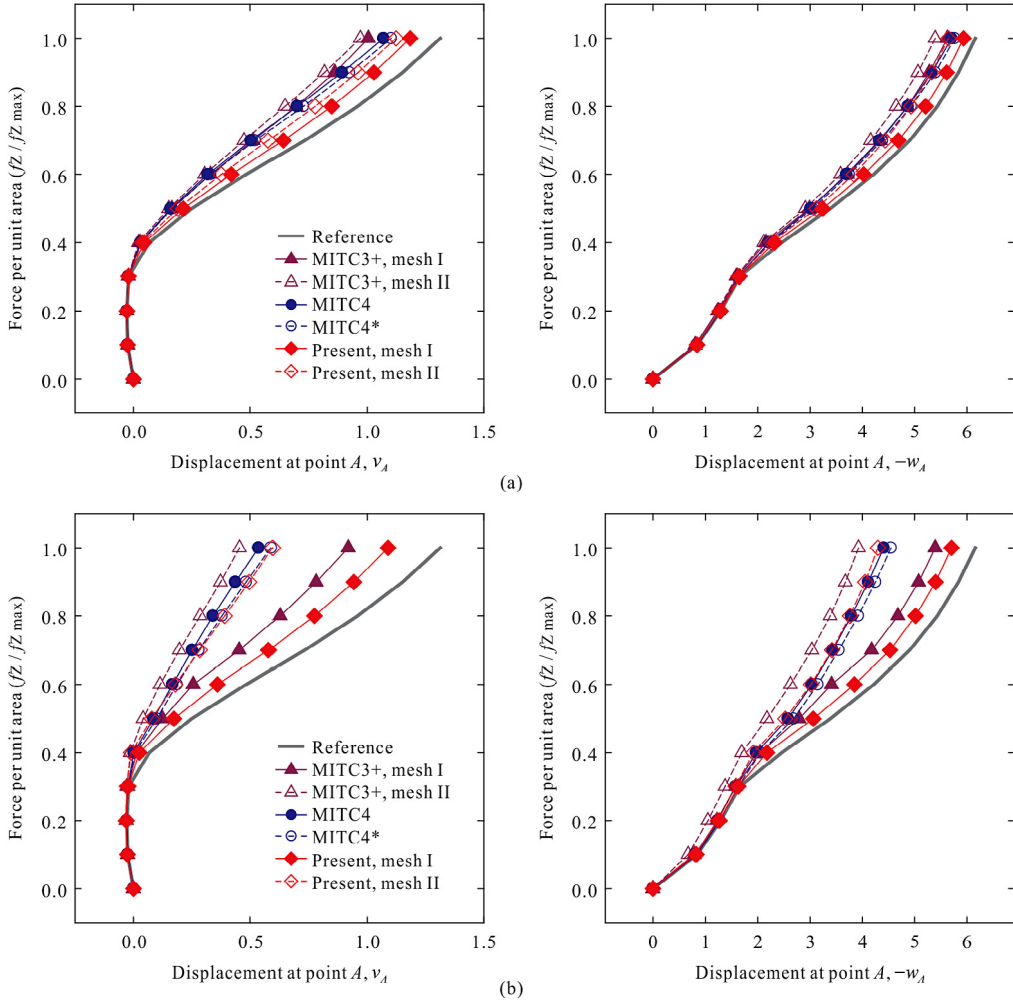


**Fig. 17.** Calculated load–displacement curves for the Scordelis–Lo roof using (a) uniform and (b) distorted meshes.

#### 4.2.4. Scordelis–Lo roof

We also study the Scordelis–Lo roof problem shown in Fig. 9(a) in a nonlinear range. The same geometry and material properties are used as in the linear analysis. The self-weight loading is now incrementally increased up to  $f_{z \max} = 50 \times 90$  per unit area. The solutions are obtained with a  $14 \times 14$  element mesh of the MITC3+, MITC4, MITC4\*, and present shell elements. The reference solution is calculated using a  $24 \times 24$  mesh of MITC9 shell elements. The two mesh patterns shown in Fig. 9(b) are considered for the triangular shell elements.

Fig. 17 shows the load–displacement curves when using the uniform and distorted mesh patterns shown in Fig. 7. As seen from the plot, the present element exhibits the best performance, even with the distorted meshes. With a  $14 \times 14$  uniform mesh of the present element, the deformed configurations of the roof structure for various load steps are shown in Fig. 18.

#### 4.2.5. Slit annular plate

The slit annular plate as shown in Fig. 19(a) is considered in this analysis. This example was suggested by Başar and Ding [44] and has been widely considered to assess the performance of shell elements in geometric nonlinear analysis. The geometry and material properties are:  $R_i = 6$ ,  $R_e = 10$ ,  $h = 0.03$ ,  $E = 21 \times 10^6$ , and  $\nu = 0$ . The lifting line force  $p_{\max} = 3.2$  per length is incrementally applied at one end of the slit, while the other end of the slit is fully clamped. The plate undergoes large displacements and large rotations.

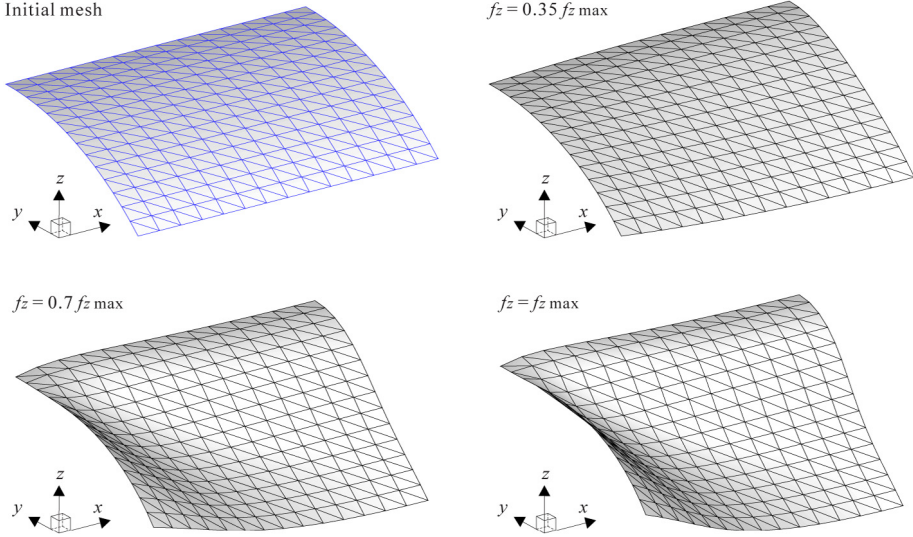


**Fig. 18.** Predicted deformed configurations for the Scordelis–Lo roof.

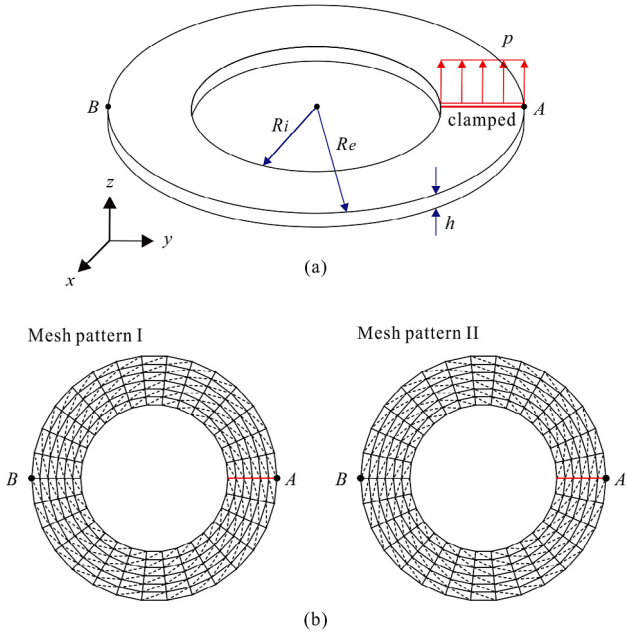


**Fig. 19.** Slit annular plate subjected to a lifting line force: (a) Problem description, (b) Mesh patterns I and II used for the triangular shell elements.

This plate is modeled using a  $6 \times 30$  mesh of the MITC4 and MITC4\* shell elements, and a corresponding mesh of the MITC3+ and present shell elements, see Fig. 19(b). To obtain the reference solutions, a  $12 \times 60$  mesh of MITC9 shell elements is employed. The load–displacement curves for two different points, A and B, are depicted in Fig. 20. The deformed configurations calculated using the MITC3+, MITC4 and present shell elements are shown in Fig. 21. The use of the present shell element yields predictions comparable to the 4-node shell elements.

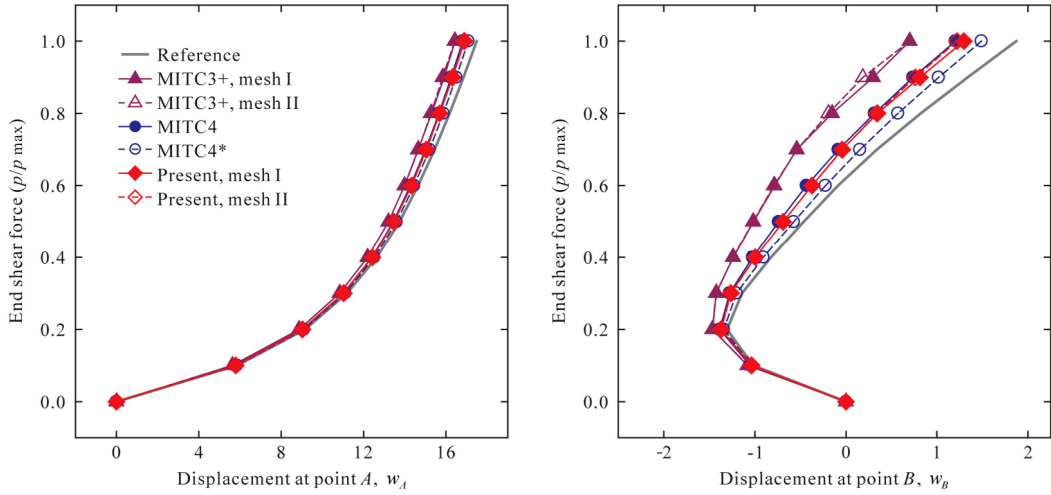


**Fig. 20.** Calculated load–displacement curves for the slit annular plate subjected to a lifting line force.

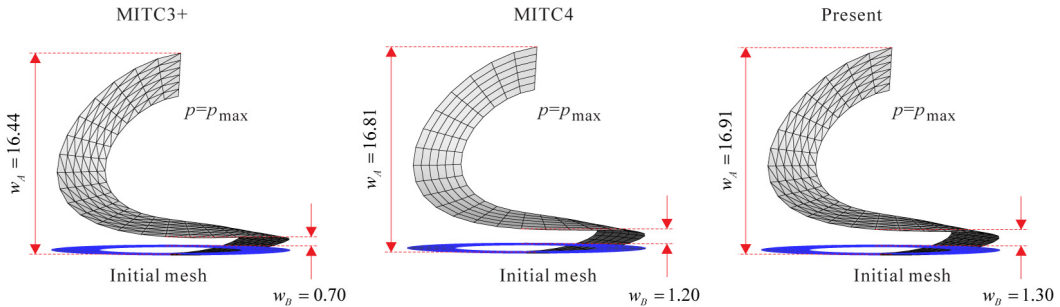


**Fig. 21.** Predicted deformed configurations for the slit annular plate subjected to a lifting line force.

## 5. Computational efficiency

In this section, we investigate some important aspects of the computational efficiency when using the improved MITC3+ shell element. The computational cost of the element is compared to that of the mixed interpolated 3- and 6-node triangular shell elements, the MITC3 and MITC6 elements [1], and the MITC3+ shell element [2–4].

Because the 6-node shell element can be curved allowing for coupling between bending and membrane behaviors, assumed membrane strains are used to reduce membrane locking [1]. This additional treatment increases the computational cost of the process, especially for nonlinear analysis. Note that such treatment is not used for the present shell element.

The number of non-zero entries in the stiffness matrix of the improved MITC3+ shell element is substantially larger than in the corresponding matrix of the 6-node shell element. This larger number is a result of the additional degrees of freedom enriching the membrane displacements at node  $i$  for the complete cover region  $C_i$  which induces a larger bandwidth and more coupling. However, for the improved MITC3+ shell element all 27 element degrees of freedom are only associated with the element vertex nodes whereas for the 6-node shell element also mid-side nodes are used. As a consequence, the assembled stiffness matrix and the bandwidth are in general smaller than when using the 6-node shell element. Fig. 22 and Table 8 show how the number of nodal degrees of freedom increases as a function of the number of element layers used in the meshes shown in Fig. 9.

It is valuable to compare the solution times required for the shell elements considered. In all cases, of course, symmetric stiffness matrices are generated. To investigate the computational efforts needed in the respective solutions, we focus on the solution time used to solve the linear equations in direct Gauss elimination, in which the factorization

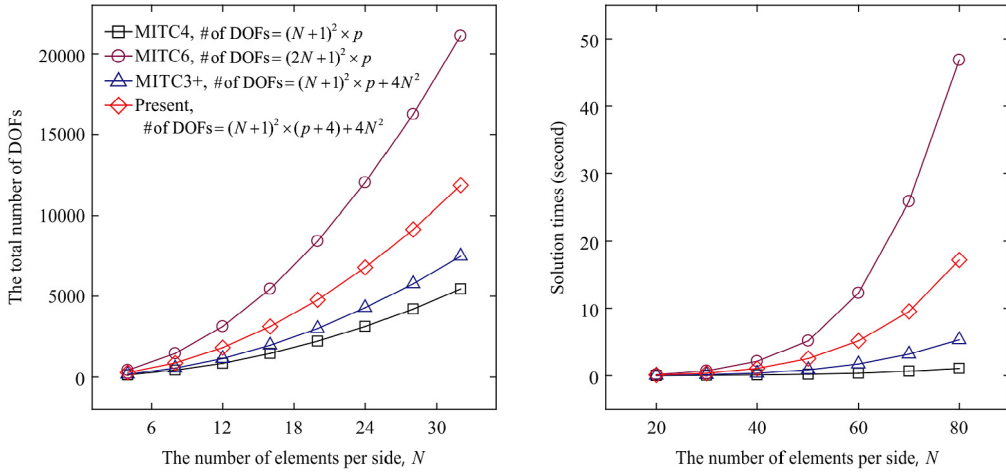


**Fig. 22.** The total number of degrees of freedom (DOFs) and solution times for solving the linear equations when increasing the number of element layers  $N$ , along the edges for the Scordelis–Lo roof problem shown in Fig. 9 ( $p$  denotes the number of shell standard DOFs ( $u, v, w, \alpha, \beta$ ) per node, hence  $p = 5$ ).

**Table 8**

Solution times (in seconds) for the Gauss equation solution of the linear problem shown in Fig. 9. (DOFs: degrees of freedom.) The value in parentheses is seen after the degrees of freedom corresponding to the bubble function are condensed out. (El. DOFs: the number of DOFs in an element.)

$N$	MITC4 shell element		MITC6 shell element		Present shell element	
	El. DOFs: $4 \times 5 = 20$		El. DOFs: $6 \times 5 = 30$		El. DOFs: $3 \times 9 + 2(\text{internal}) = 29$	
	Free DOFs	Time	Free DOFs	Time	Free DOFs	Time
20	2,080	<0.000	8,160	0.140	5,320 (3,720)	0.062 (0.031)
40	8,160	0.078	32,320	2.122	21,040 (14,640)	1.045 (0.374)
60	18,240	0.359	72,480	12.29	47,160 (32,760)	5.101 (1.731)
80	32,320	1.045	128,640	46.85	83,680 (58,080)	17.20 (5.335)

of the stiffness matrix represents the major expense. We use a quad-core machine (Intel(R) Core i7-3770 CPU @ 3.40 GHz, 8 GB RAM, Windows 7 64bit) for all solutions. Fig. 22 and Table 8 show the solution times for the linear analysis of the Scordelis–Lo roof problem. As expected, when a symmetric skyline solver is used, the time using the improved MITC3+ shell element is much smaller than for the 6-node triangular shell element. Of course, to establish a thorough comparison also the accuracy achieved in the respective solutions should be considered.

## 6. Concluding remarks

We proposed a significant improvement of the MITC3+ shell element reached by enriching its membrane displacements. As a consequence, the element has 9 degrees of freedom, instead of the usual five, at each of the three corner nodes. We presented the formulations for linear and geometric nonlinear analyses, and observed an excellent element performance in the analysis of various linear and geometric nonlinear test problems, even with the use of distorted meshes. Hence the element is quite attractive for the analysis of general shell structures.

## Acknowledgments

This work was supported by the National Research Foundation of Korea (NRF) grant funded by the Korea government (MSIT) (No. NRF-2018R1A2B3005328). We also thank San Kim at Korea Advanced Institute of Science and Technology (KAIST) for his valuable comments.

## References

- [1] P.S. Lee, K.J. Bathe, Development of MITC isotropic triangular shell finite elements, *Comput. Struct.* 82 (2004) 945–962.
- [2] Y. Lee, P.S. Lee, K.J. Bathe, The MITC3+ shell element and its performance, *Comput. Struct.* 138 (2014) 12–23.
- [3] H.M. Jeon, Y. Lee, P.S. Lee, K.J. Bathe, The MITC3+ shell element in geometric nonlinear analysis, *Comput. Struct.* 146 (2015) 91–104.
- [4] Y. Lee, H.M. Jeon, P.S. Lee, K.J. Bathe, The modal behavior of the MITC3+ triangular shell element, *Comput. Struct.* 153 (2015) 148–164.
- [5] P.S. Lee, H.C. Noh, K.J. Bathe, Insight into 3-node triangular shell finite elements: the effects of element isotropy and mesh patterns, *Comput. Struct.* 85 (2007) 404–418.
- [6] K.J. Bathe, *Finite Element Procedures*, second ed., K.J. Bathe, Watertown, 2014 and Higher Education Press, China, 2016.
- [7] T.J.R. Hughes, *The Finite Element Method: Linear Static and Dynamic Finite Element Analysis*, Dover Publications, Mineola, NY, 2000.
- [8] O.C. Zienkiewicz, R.L. Taylor, J.M. Too, Reduced integration technique in general analysis of plates and shells, *Internat. J. Numer. Methods Engrg.* 3 (1971) 275–290.
- [9] D. Chapelle, K.J. Bathe, *The Finite Element Analysis of Shells—Fundamentals*, second ed., Springer, 2011.
- [10] D. Chapelle, K.J. Bathe, Fundamental considerations for the finite element analysis of shell structures, *Comput. Struct.* 66 (1998) 19–36.
- [11] U. Andelfinger, E. Ramm, EAS-elements for two-dimensional, three-dimensional, plate and shell structures and their equivalence to HR-elements, *Internat. J. Numer. Methods Engrg.* 36 (1993) 1311–1337.
- [12] J.C. Simo, M.S. Rifai, A class of mixed assumed strain methods and the method of incompatible modes, *Internat. J. Numer. Methods Engrg.* 29 (1990) 1595–1638.
- [13] K.J. Bathe, E.N. Dvorkin, A formulation of general shell elements—the use of mixed interpolation of tensorial components, *Internat. J. Numer. Methods Engrg.* 22 (1986) 697–722.
- [14] T. Belytschko, C. Tsay, A stabilization procedure for the quadrilateral plate element with one-point quadrature, *Internat. J. Numer. Methods Engrg.* 19 (1983) 405–419.
- [15] R.H. MacNeal, Derivation of element stiffness matrices by assumed strain distributions, *Nucl. Eng. Des.* 70 (1982) 3–12.
- [16] C.M. Shin, B.C. Lee, Development of a strain-smoothed three-node triangular flat shell element with drilling degrees of freedom, *Finite Elem. Anal. Des.* 86 (2014) 71–80.
- [17] T. Nguyen-Thoi, P. Phung-Van, C. Thai-Hoang, H. Nguyen-Xuan, A cell-based smoothed discrete shear gap method (CS-DSG3) using triangular elements for static and free vibration analyses of shell structures, *Int. J. Mech. Sci.* 74 (2013) 32–45.
- [18] Y. Ko, P.S. Lee, K.J. Bathe, A new 4-node MITC element for analysis of two-dimensional solids and its formulation in a shell element, *Comput. Struct.* 192 (2017) 34–49.
- [19] R.L. Taylor, P.J. Beresford, E.L. Wilson, A non-conforming element for stress analysis, *Internat. J. Numer. Methods Engrg.* 10 (1976) 1211–1219.
- [20] E.L. Wilson, A. Ibrahimbegovic, Use of incompatible displacement modes for the calculation of element stiffnesses or stresses, *Finite Elem. Anal. Des.* 7 (1990) 229–241.
- [21] C.A. Felippa, A study of optimal membrane triangles with drilling freedoms, *Comput. Methods Appl. Mech. Engrg.* 192 (2003) 2125–2168.
- [22] J.M. Melenk, I. Babuška, The partition of unity finite element method: basic theory and applications, *Comput. Methods Appl. Mech. Engrg.* 139 (1996) 289–314.
- [23] C.A. Duarte, I. Babuška, J.T. Oden, Generalized finite element methods for three-dimensional structural mechanics problems, *Comput. Struct.* 77 (2000) 215–232.
- [24] Y. Cai, X. Zhuang, C. Augarde, A new partition of unity finite element free from the linear dependence problem and possessing the delta property, *Comput. Methods Appl. Mech. Engrg.* 199 (2010) 1036–1043.
- [25] J.P. Xu, S. Rajendran, A “FE-meshfree” TRIA3 element based on partition of unity for linear and geometry nonlinear analyses, *Comput. Mech.* 51 (2013) 843–864.
- [26] R. Tian, Extra-dof-free and linearly independent enrichments in GFEM, *Comput. Methods Appl. Mech. Engrg.* 266 (2013) 1–22.
- [27] J. Kim, K.J. Bathe, The finite element method enriched by interpolation covers, *Comput. Struct.* 116 (2013) 35–49.
- [28] J. Kim, K.J. Bathe, Towards a procedure to automatically improve finite element solutions by interpolation covers, *Comput. Struct.* 131 (2014) 81–97.
- [29] H.M. Jeon, P.S. Lee, K.J. Bathe, The MITC3 shell finite element enriched by interpolation covers, *Comput. Struct.* 134 (2014) 128–142.
- [30] R. Tian, G. Yagawa, H. Terasaka, Linear dependence problems of partition of unity-based generalized FEMs, *Comput. Methods Appl. Mech. Engrg.* 195 (2006) 4768–4782.
- [31] K.J. Bathe, E. Ramm, E.L. Wilson, Finite element formulations for large deformation dynamic analysis, *Internat. J. Numer. Methods Engrg.* 9 (1975) 353–386.
- [32] T. Sussman, K.J. Bathe, Spurious modes in geometrically nonlinear small displacement finite elements with incompatible modes, *Comput. Struct.* 140 (2014) 14–22.
- [33] K.Y. Sze, D. Zhu, A quadratic assumed natural strain curved triangular shell element, *Comput. Methods Appl. Mech. Engrg.* 174 (1999) 57–71.
- [34] K.U. Bletzinger, M. Bischoff, E. Ramm, A unified approach for shear-locking-free triangular and rectangular shell finite elements, *Comput. Struct.* 75 (2000) 321–334.
- [35] K.J. Bathe, P.S. Lee, J.F. Hiller, Towards improving the MITC9 shell element, *Comput. Struct.* 81 (2003) 477–489.
- [36] T.H.H. Pian, K. Sumihara, Rational approach for assumed stress finite elements, *Internat. J. Numer. Methods Engrg.* 20 (1984) 1685–1695.
- [37] J.C. Simo, D.D. Fox, On a stress resultant geometrically exact shell model. Part I: Formulation and optimal parametrization, *Comput. Methods Appl. Mech. Engrg.* 72 (1989) 267–304.

- [38] T. Belytschko, I. Leviathan, Physical stabilization of the 4-node shell element with one point quadrature, *Comput. Methods Appl. Mech. Engrg.* 113 (1994) 321–350.
- [39] R.H. MacNeal, A simple quadrilateral shell element, *Comput. Struct.* 8 (1978) 175–183.
- [40] T. Belytschko, B.L. Wong, H. Stolarski, Assumed strain stabilization procedure for the 9-node Lagrange shell element, *Internat. J. Numer. Methods Engrg.* 28 (1989) 385–414.
- [41] R.D. Cook, *Concepts and Applications of Finite Element Analysis*, John Wiley & Sons, 2007.
- [42] R.H. MacNeal, R.L. Harder, A proposed standard set of problems to test finite element accuracy, *Finite Elem. Anal. Des.* 1 (1985) 3–20.
- [43] P.S. Lee, K.J. Bathe, On the asymptotic behavior of shell structures and the evaluation in finite element solutions, *Comput. Struct.* 80 (2002) 235–255.
- [44] Y. Başar, Y. Ding, Finite-rotation shell elements for the analysis of finite-rotation shell problems, *Internat. J. Numer. Methods Engrg.* 34 (1992) 165–169.